JOURNAL OF GEOPHYSICAL RESEARCH, VOL. 99, NO. D3, PAGES 5499–5514, MARCH 20, 1994

Multilevel cloud retrieval using multispectral HIRS and AVHRR data: Nighttime oceanic analysis

Bryan A. Baum,[1] Robert F. Arduini,[2] Bruce A. Wielicki,[1] Patrick Minnis,[1] and Si-Chee Tsay[3]

Abstract. A multispectral, multiresolution (MSMR) method is developed for analyzing scenes of overlapping cloud layers. The MSMR method is applied to data from the NOAA 11 advanced very high resolution radiometer (AVHRR) and the high-resolution infrared radiometer sounder (HIRS-2). The data are from a nighttime oceanic scene in which a semitransparent cirrus veil overlays a large-scale stratus cloud. Low-cloud and clear-sky radiances are determined using a spatial coherence technique. Middle to upper level cloud pressures and radiances are estimated from HIRS-2 15-μm CO_2 band radiometric data. The MSMR method improves the interpretation of a nighttime, oceanic scene containing thin cirrus over a large-scale stratiform cloud. If, for example, the same scene is analyzed using only the AVHRR 10.8-μm channel, the accompanying retrieved cloud heights are found to be between the cirrus and stratus cloud heights and are incorrectly identified as midlevel altostratus clouds. Theoretical radiative transfer model results for both water droplet spheres and randomly oriented hexagonal ice crystals are compared to observed AVHRR brightness temperature differences (BTD) between the 3.7- and 10.8-μm channels (BTD^{34}) and between the 10.8- and 12-μm channels (BTD^{45}) to distinguish among the effects of cloud optical depth, particle size, and phase for both single-layer clouds and overlapping two-layer clouds. Theoretical BTD calculations are used to estimate the range of effective particle sizes for each cloud layer. The data for the cirrus in the case study region near Bermuda are consistent with theoretical results for relatively small randomly oriented hexagonal ice crystals. The observed BTD^{34} and BTD^{45} values are lower for the cirrus above a lower-level cloud than for single-level cirrus with no underlying cloud. In certain cases the BTD analysis provides a way to distinguish between clouds composed of supercooled water droplets rather than ice particles. Analysis of nighttime data permits determination of stratus infrared optical depths smaller than 4.

1. Introduction

To be successful in understanding and modeling the Earth's climate, we must understand the influence of clouds. The importance of clouds in determining the Earth's radiation budget at the top of the atmosphere was demonstrated using data from the Earth Radiation Budget Experiment (ERBE) [e.g., *Ramanathan et al.*, 1989; *Harrison et al.*, 1990]. *Cess et al.* [1990] performed intercomparisons among 19 general circulation models (GCMs) that differed in the parameterizations of clouds and their radiative properties. *Cess et al.* [1990] concluded that the role of clouds is still rather poorly understood since the models may produce similar climate sensitivities as a consequence of different cloud feedback components, such as changes in cloud fraction or cloud height. While clouds have a large effect on the radiation budget at the top of the atmosphere, clouds are also important in determining the surface radiation budget (SRB) as well as the distribution of energy throughout the atmosphere. For example, the downward longwave flux depends on the vertical cloud structure and the cloud base heights [*Gupta et al.*, 1992]. To test the validity of cloud parameterizations in both GCM and SRB models, it is essential to have a global cloud climatology, a problem that is being addressed by the International Satellite Cloud Climatology Project (ISCCP) [*Schiffer and Rossow*, 1983]. The ISCCP cloud retrieval algorithm uses one visible and one infrared (IR) channel in a relatively simple bispectral technique that cannot adequately address some cloud characteristics, such as vertical structure and semitransparency, especially at night when only the IR data are available. The present work concentrates on the detection and interpretation of satellite observations of scenes containing overlapping clouds.

Current satellite cloud retrieval algorithms estimate cloud parameters such as height, fractional coverage, and extinction optical depth for a single layer of cloud, but the analysis of overlapping cloud layers remains largely unexplored. Surface observations and satellite imagery show that multilayered cloud systems are commonly found in frontal areas where cirrus overlays boundary layer convective cloud or stratus cloud. A summary of 12 years (1965–1976) of ship-reported synoptic observations [*Hahn et al.*, 1982] over the North Atlantic Ocean shows that cirrus clouds have a frequency of occurrence between 20 and 45%, depending

[1]Atmospheric Sciences Division, NASA Langley Research Center, Hampton, Virginia.
[2]Lockheed Engineering and Sciences Corporation, Hampton, Virginia.
[3]NASA Goddard Space Flight Center, Greenbelt, Maryland.

Paper number 93JD02856.
0148-0227/94/93JD-02856$05.00

Table 1. NOAA 11 HIRS and AVHRR Channels, Central Wavelengths, Principal Absorbing Components, and Approximate Pressure Level Corresponding to the Peak in the Individual Channel Weighting Functions

Instrument	Channel Number	Central Wavelength, μm	Principal Absorbing Component	Approximate Peak in Weighting Function, mbar
HIRS	4	14.21	CO_2	300
HIRS	5	13.95	CO_2	500
HIRS	6	13.66	CO_2; H_2O	750
HIRS	7	13.34	CO_2; H_2O	900
HIRS	8	11.10	H_2O	surface
AVHRR	3	3.73	H_2O	surface
AVHRR	4	10.8	H_2O	surface
AVHRR	5	12.0	H_2O	surface

HIRS, high-resolution infrared radiometer sounder; AVHRR, advanced very high resolution radiometer.

upon season and location. The frequency of stratus co-occurrence with cirrus is often greater than 50% between 30°N and 60°N, also depending upon season and location. *Hahn et al.* [1982] also show that in the 30°–60°N region the probability of finding cirrus over ocean with no other cloud present is usually less than 20%. *Tian and Curry* [1989], in a study of cloud overlap statistics performed using Air Force three-dimensional nephanalysis during January 1979 over the North Atlantic Ocean between 40° and 60°N, also found that cirrus have a high co-occurrence with stratus. In that study, Tian and Curry found that cirrus frequency of occurrence was 22%, the probability of stratus co-occurrence with cirrus was 61%, and the frequency of finding cirrus with no other clouds present was 7%. Given the relatively high probability of finding cirrus with other cloud types and the low probability of finding cirrus alone, we turn to the problem of how to infer the vertical cloud structure prevalent over oceans using National Oceanic and Atmospheric Administration (NOAA) operational satellite data.

The multilevel cloud analysis is accomplished through the use of merged high-resolution infrared radiation sounder (HIRS-2, henceforth HIRS) and advanced very high resolution radiometer (AVHRR) data. Both the HIRS and the AVHRR radiometers are flown on the NOAA series of polar-orbiting platforms. In section 2 we extend the multispectral, multiresolution (MSMR) method [*Baum et al.*, 1992] by implementing the spatial coherence method [*Coakley and Bretherton*, 1982; *Coakley*, 1983]. When applied to the AVHRR imaging data, the spatial coherence method determines whether a stratus cloud may be present and the mean radiance and corresponding pressure level of the stratus layer. The stratus cloud pressure then is used in subsequent analysis of the HIRS 15-μm data to determine a more accurate upper cloud height. The multiple-scattering radiative transfer model, described further in section 3, is used to simulate relationships between the (3.7–10.8 μm) and (10.8–12 μm) brightness temperature differences (BTD^{34} and BTD^{45}, respectively) as functions of cloud particle effective radius r_{eff}, infrared optical depth τ, and 10.8-μm brightness temperature. Theoretical results are presented and discussed in section 4. In section 5 we present a case study of multilevel clouds in the vicinity of Bermuda. Discussion of the results of this study are detailed in section 6, and our conclusions are outlined in section 7.

2. Methodology

2.1. Satellite Data

High-resolution (1.1 km) AVHRR data from the Sun-synchronous NOAA 11 satellite are used in this study. The NOAA 11 satellite has nominal equator crossing times of 0730 and 1930 local solar time (LST). The AVHRR instrument is comprised nominally of five channels, of which three are used for nighttime analysis as shown in Table 1. Near-infrared (NIR) and IR radiances are calculated from the raw counts provided in the NOAA 1B data stream using the nominal calibration [*Kidwell*, 1991] and the nonlinearity corrections of *Weinreb et al.* [1990].

HIRS radiometric data are also used in this investigation. The HIRS radiometric sounding unit is one of the components that make up the TIROS operational vertical sounder (TOVS) instrument package. The HIRS instrument [*Koenig*, 1980] receives visible and infrared radiation through a single telescope and splits the radiation into 19 narrowband infrared channels and 1 visible narrowband channel by means of a rotating filter wheel. The HIRS channels used in this work and some of their characteristics are detailed in Table 1. The HIRS pixel instantaneous field of view (FOV) enlarges from 17.4 km at nadir to 30 km × 58 km toward the edge of the scan line.

2.2. Multispectral, Multiresolution (MSMR) Method

Baum et al. [1992] described an MSMR method that merges AVHRR data with individual HIRS pixels. The method accounted for the fact that there are gaps between individual HIRS FOVs both within and between scan lines due to the design of the instrument. To fully implement the spatial coherence technique, all of the AVHRR pixels should be used, not just those collocated with an individual HIRS FOV. The MSMR technique outlined by *Baum et al.* [1992] has been modified herein to use all of the AVHRR data, not just the AVHRR data collocated with each HIRS FOV, and now superimposes the HIRS FOVs over the AVHRR imaging data.

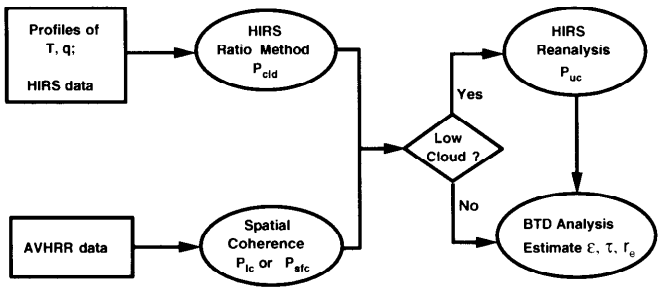

Figure 1. Schematic of HIRS/AVHRR data processing procedure. Spatial coherence is used to determine clear-sky radiance and lower-cloud radiance, if present. HIRS ratio method uses results of spatial coherence to determine theoretical radiance profiles used in the ratio method. Radiative transfer theory is used to estimate phase and effective radius of each cloud layer.

The improved algorithm is shown schematically in Figure 1. HIRS 15-μm radiometric data are analyzed in conjunction with the AVHRR radiometric data. The spatial coherence algorithm is applied to the AVHRR 10.8-μm data collected within a chosen subregion to determine the mean radiance of the lower cloud layer. An implicit assumption in the spatial coherence technique is that the clouds have an emittance of 1. With this assumption we relate the radiance of the lower cloud and hence its brightness temperature to a physical temperature for use in the theoretical radiative transfer calculations. If the cloud were to have an emittance less than 1, the spatial coherence technique would retrieve a lower than actual cloud top height. If a lower cloud deck is present, the lowest emitting surface in the HIRS algorithm is redefined to be the lower cloud top pressure as determined from spatial coherence analysis. This approach primarily affects the HIRS cloud height retrievals for those pixels that contain optically thin cloud [*Baum and Wielicki*, 1994].

2.3. High-Resolution Infrared Radiometer Sounder (HIRS) Analysis

The CO_2 slicing methods [e.g., *McCleese and Wilson*, 1976; *Smith and Platt*, 1978; *Chahine*, 1974] have been applied to radiometric data from several instruments, notably the HIRS, the visible and infrared spin scan radiometer (VISSR) atmospheric sounder (VAS) [e.g., *Menzel et al.*, 1983; *Wylie and Menzel*, 1989], and most recently to the high-resolution interferometer sounder (HIS) [*Smith and Frey*, 1990]. The CO_2 slicing methods provide an accurate means of inferring middle- to high-level cloud pressure from passive infrared 15-μm channel spectral radiance measurements. Each of the 15-μm CO_2 sounding channels are spaced closely in wavenumber and have varying opacity to CO_2, with the result that each channel is sensitive to a different level in the atmosphere. The pressure level of peak energy contribution for each HIRS channel is determined by the weighting function, dt/d (ln P), where t is transmission and P is pressure. In general, the peak of both sounding-channel weighting functions should be at or below the cloud height to be retrieved. The pressure level corresponding to the peak in the individual satellite channel weighting functions are provided in Table 1. One constraint on the HIRS algorithm is that at cloud pressures greater than approximately 700 mbar, i.e., low cloud, bias errors become important and tend to place clouds at a lower pressure (higher in the atmosphere) than they actually are. In addition, the signal to noise ratio for the sounding channels decreases rapidly for clouds below 700 mbar, to the point where low-level cloud pressure retrievals are problematic [*Wielicki and Coakley*, 1981].

We expect significant cloud height retrieval errors if the HIRS FOV contains low clouds and upper cloud that is semitransparent. Two recent studies [*Menzel et al.*, 1992; *Baum and Wielicki*, 1994] describe more quantitatively the errors which occur when more than one cloud layer is present in the radiometer FOV. The exact amount of upper cloud pressure retrieval error depends on the emittance of both the upper (*uc*) and the lower (*lc*) cloud layers. The cloud pressure retrieval error increases with decreasing upper cloud layer effective cloud amount, defined as the emittance ε multiplied by the upper cloud fraction A_{uc}. *Baum and Wielicki* [1994], when considering random and bias errors due to instrument noise and overlapping clouds, show that the optimal HIRS channel combination depends upon whether the aim is to minimize random errors or minimize bias errors. While the sounding channels that peak between 700 and 1000 mbar minimize random errors, the sounding channels that peak between 300 and 500 mbar minimize bias errors. We follow the scheme outlined by *Baum and Wielicki* [1994] in an effort to reduce instantaneous error, i.e., using the HIRS 4/5 channel combination for cirrus at pressures less than about 300 mbar and the HIRS 6/7 channel combination for cloud pressures larger than about 350 mbar. Details are provided by *Baum and Wielicki* [1994] regarding the development of the HIRS CO_2 slicing algorithm for retrieval of the upper cloud pressure for a two-layer cloud scenario.

2.4. Determination of Clear-Sky and Lower-Cloud Radiances

The accuracy of cloud retrieval algorithms depends in large part upon the clear-sky radiance. In this study, our approach is to use the spatial coherence method detailed by *Coakley and Bretherton* [1982] and *Coakley* [1983]. The basic technique employed is to use the local spatial structure of the AVHRR 10.8-μm radiance field to identify regions that contain spatially uniform clear-sky or cloud radiances. The method determines the properties of optically thick clouds that cover an areal extent much greater than the individual pixel size and requires both completely cloud-covered and completely clear fields of view.

Once clear-sky oceanic regions have been identified, the sea surface temperature is determined from a linear multichannel sea surface temperature (MCSST) algorithm [*McClain et al.*, 1985] but using coefficients in the algorithm determined specifically for NOAA 11 (C. C. Walton, personal communication, 1993).

3. Radiative Transfer Theory and Models

3.1. Microphysical Models

Stratiform clouds composed of water droplets are modeled using a gamma size distribution [*Hansen and Travis*, 1974] for effective radii r_{eff} of 4, 8, and 16 μm and an effective variance v_{eff} of 0.1 for all cases. For each droplet distribution the phase function and the scattering, absorption, and extinction cross sections are computed using Mie scattering theory [*Wiscombe*, 1980]. The single-scattering albedo $\tilde{\omega}$, the

Table 2. Microphysical Parameters and Optical Properties Used in the Calculations for Mie Scattering Using a Gamma Distribution of Water Droplets

r_{eff}, μm	Wavelength, μm	$\tilde{\omega}$	C_{abs}, μm^2	C_{ext}, μm^2
4.0	3.73	0.96728	3.76	114.92
	10.82	0.32827	17.83	26.54
	12.00	0.22182	29.26	37.60
8.0	3.73	0.91725	28.57	345.26
	10.82	0.47900	112.96	216.81
	12.00	0.35239	152.00	234.70
16.0	3.73	0.85656	186.21	1298.20
	10.82	0.54276	591.01	1292.54
	12.00	0.44098	658.08	1177.20

Calculations are performed for the NOAA 11 AVHRR near-infrared (NIR) and IR wavelengths. The complex refractive indices of water are taken from *Downing and Williams* [1975] and are $m = 1.37–0.00348i$ at $\lambda = 3.73$ μm, $m = 1.16–0.0868i$ at $\lambda = 10.8$ μm, and $m = 1.13–0.203i$ at $\lambda = 12$ μm.

absorption cross section, C_{abs}, and the extinction cross section, C_{ext}, are listed in Table 2 as a function of r_{eff}.

Cirrus clouds are modeled as randomly oriented hexagonal ice crystals. The ice crystal optical properties and phase functions from *Liou et al.* [1990] and *Minnis et al.* [1993] are used at wavelengths of 3.7 and 10.8 μm, respectively. A comparison of the scattering phase function at 10 μm [*Liou et al.*, 1990] to the phase function at 10.8 μm shows that at 10.8 μm the peak at a scattering angle of approximately 30° tends to smooth out. We expect the phase function to be fairly uniform throughout the window region, and for this reason the 10.8-μm scattering phase function is used for both the 10.8-μm and the 12-μm calculations. As noted by *Takano et al.* [1992], the single-scattering albedo and optical properties for the hexagonal ice crystals can be parameterized in terms of the area-equivalent size parameter, $\chi_e = 2\pi r_g/\lambda$, where r_g is the radius of the area-equivalent sphere. Parameterizations for large crystals may be used to derive single-scattering albedo and extinction efficiency when the size parameter is above 20 and 30, respectively. At smaller-size parameters the single-scattering albedo and extinction efficiency can be estimated using a spheroid model for small crystals [*Takano et al.*, 1992]. The single-scattering and extinction cross-section properties are shown in Table 3 for ice crystals having five different aspect ratios. As noted from the area-equivalent size parameters for each of these ice crystals, the single-scattering albedos and extinction cross sections for the hexagonal ice crystals having aspect ratios of 20/20, 50/40, and 120/60 are calculated by using the small crystal approximation of *Takano et al.* [1992] at wavelengths of 10.8 and 12 μm. The aspect ratio is $L/2a$, where L is the length of the crystal and $2a$ is the width of the crystal. In the large-particle limit, the extinction cross sections are independent of wavelength.

3.2. Radiative Transfer Models

The radiative transfer model used for the solution of the radiative transfer equation is an optimized form of the discrete ordinate method and includes the effects of multiple scattering, absorption, and emission within an atmospheric column. The method, first proposed by *Chandrasekhar* [1960], has been further developed and discussed in the literature [*Liou*, 1973; *Stamnes et al.*, 1988; *Tsay et al.*, 1990]. The discrete ordinates method, subsequently referred to as the discrete ordinates radiative transfer (DISORT) model, assumes that the atmosphere consists of a number of adjacent homogeneous layers in which the single-scattering properties are constant within each layer but may vary from layer to layer. The ability to have different scattering properties in each atmospheric layer makes DISORT useful in the investigation of the properties of overlapping cloud scenarios. DISORT calculations require a phase function, single-scattering albedo, IR optical depth, and temperature for each layer. LOWTRAN-7 [see *Kneizys et al.*, 1988] is used to develop the clear-sky optical depth profile that includes the effect of atmospheric absorbers such as H_2O, CH_4, O_3,

Table 3. Microphysical Parameters and Optical Properties Used in the Theoretical Calculations for Randomly Oriented Hexagonal Ice Crystals

$L/2a$	Wavelength, μm	χ_e	C_{ext}, μm^2	$\tilde{\omega}$
20/20	3.73	19.9	6.54 (+2)	0.8382
	10.82	6.8	5.47 (+2)	0.3435
	12.00	6.1	7.43 (+2)	0.4209
50/40	3.73	43.1	4.04 (+3)	0.7263
	10.8	14.8	3.03 (+3)	0.4299
	12.0	13.3	3.35 (+3)	0.4661
120/60	3.73	77.6	1.31 (+4)	0.6671
	10.8	26.6	1.01 (+4)	0.4691
	12.0	23.9	1.07 (+4)	0.5033
300/100	3.73	153.7	5.15 (+4)	0.6064
	10.8	52.7	5.15 (+4)	0.5300
	12.0	47.4	5.15 (+4)	0.5300
750/160	3.73	300.4	1.97 (+5)	0.5656
	10.8	102.9	1.97 (+5)	0.5300
	12.0	92.6	1.97 (+5)	0.5300

The symbols $L/2a$, χ_e, $\tilde{\omega}$, and C_{ext} refer to hexagonal ice crystal aspect ratio, area-equivalent size parameter, single-scattering albedo, and extinction cross section, respectively. The complex refractive indices of ice, taken from *Warren* [1984], are $m = 1.395–0.0069i$ at $\lambda = 3.73$ μm, $m = 1.089–0.183i$ at $\lambda = 10.8$ μm, and $m = 1.280–0.4133i$ at $\lambda = 12$ μm.

N_2O, CO, and CO_2 at the specified levels in the atmosphere. In situ temperature and relative humidity profiles are used as input to the LOWTRAN-7 calculations. Calculations for the AVHRR NIR and IR channels are performed for a central wavelength only.

The problem solved here is of a lower-emitting surface having an emittance of 1 with two overlapping cloud layers within an absorbing, emitting, and scattering atmosphere. An aerosol contribution is included in our simulations. The aerosol profile comes from the LOWTRAN-7 maritime aerosol for the boundary layer (0–2 km) having a "meteorological range" (roughly equivalent to the visibility) of 23 km and also the LOWTRAN-7 background stratospheric aerosol profile for the upper atmosphere. The lower stratus cloud layer is defined by one of the water droplet models in Table 2. The cirrus cloud layer is assumed to be composed of one of the single-size, randomly oriented, hexagonal ice crystals in Table 3. The 10.8-μm optical depths of both upper and lower cloud layers span a range from 0.1 to 50. The corresponding optical depths at 3.7 and 12 μm are scaled according to the ratio of the extinction cross sections, e.g.,

$$\tau(3.7\ \mu\text{m}) = \frac{C_{\text{ext}}(3.7\ \mu\text{m})}{C_{\text{ext}}(10.8\ \mu\text{m})}\,\tau(10.8\ \mu\text{m}) \qquad (1)$$

A Legendre polynomial expansion is used to represent the scattering phase function. In this version of the DISORT model, the number of streams is equal to the number of terms, or Legendre coefficients, used in the expansion. We used 16 streams for these nighttime calculations and also averaged over azimuth. The DISORT model is used to derive brightness temperature differences between the 3.7-μm and the 10.8-μm brightness temperatures and between the 10.8-μm and the 12-μm brightness temperatures at the top of the atmosphere as a function of upper and lower cloud layer infrared optical depth, temperature, and effective radius.

3.3. Interpretation of Advanced Very High Resolution Radiometer Near-Infrared (AVHRR NIR) and IR Data

The AVHRR NIR and IR channel radiances measured by the satellite include contributions from the surface, clouds, and atmosphere. In this section we review the primary influences upon the upwelling NIR and IR radiances for cloud fields at night. These influences include the nonlinearity of the Planck radiance with temperature and cloud emittance variations with wavelength.

The variation of BTD^{34} with εA_c as a function of the 10.8-μm brightness temperature can be demonstrated for a simple case of single and overlapping cloud layers. For this case, calculations are performed for cloud layers with no intervening atmosphere and further assume that the cloud emittances are equal in both the 3.7-μm and the 10.8-μm channels. The effect of the nonlinearity of the Planck radiance with temperature is shown in Figure 2. This figure shows the effect of variations in εA_c on the BTD^{34} as a function of the 10.8-μm brightness temperature for two single-layered clouds, one at 224 K and the other at 280 K. A third case is presented that shows the variation in BTD^{34} with εA_c expected when the two clouds at 280 K and 224 K overlap. For this third case, $\varepsilon A_c = 1$ for the low cloud and varies from 0 to 1 for the high cloud. It is evident from this figure that the BTD^{34} values depend very strongly on the

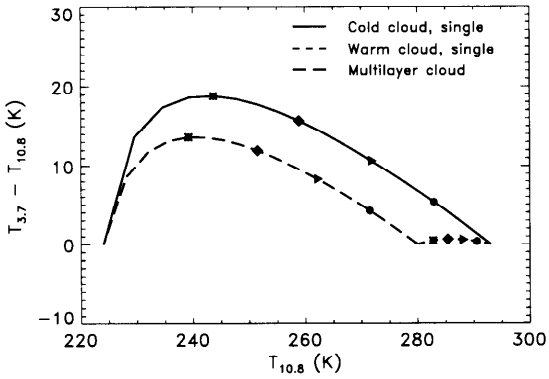

Figure 2. Dependence of BTD^{34} ($T(3.7\ \mu\text{m}) - T(10.8\ \mu\text{m})$) on effective cloud amount εA_c as a function of the 10.8-μm brightness temperature due to the nonlinearity of the Planck radiance with temperature. Calculations are performed for no atmosphere and the cloud emittances are assumed to be the same at 3.7 and 10.8 μm. Curves are shown for a single-layered warm cloud (280 K), a single-layered cold cloud (224 K), and for overlapping cloud layers. On the theoretical curves, effective cloud amount (εA_c) values of 0.2, 0.4, 0.6, and 0.8 are represented by a circle, triangle, square, and asterisk, respectively.

temperature and εA_c. Additionally, for the overlapping cloud case, the BTD^{34} values are shown to decrease from the single-level cold (224 K) cloud case because the lower boundary is the cloud at 280 K instead of the warmer surface.

In general, however, the emittances are not equal at the NIR and IR wavelengths. Due to the variation of the imaginary index of refraction with wavelength for both ice and water particles, the 3.7-μm emittances tend to be lower than at the 10.8- or 12-μm wavelengths [e.g., *Hunt*, 1973; *d'Entremont*, 1986; *Stone et al.*, 1990]. The imaginary index of refraction is about a factor of 30 lower at 3.7 μm than at 10.8 μm for ice [*Warren*, 1984] (see also Table 3) and about a factor of 25 lower at 3.7 μm than at 10.8 μm for water [*Downing and Williams*, 1975] (see also Table 2). The imaginary index of refraction of the water or ice particles may be used to calculate the absorption coefficient $k_{\text{abs}} = 4\pi c_i/\lambda$, where λ is the wavelength and c_i is the imaginary part of the complex index of refraction. The absorption coefficient may be used to calculate an absorption optical depth τ_a which, without scattering, is related to the emittance through $\varepsilon = 1 - \exp[-\tau_a]$.

The relationship between the 3.7-μm and the 10.8-μm emittances also depends on particle size [e.g., *Ackerman and Stephens*, 1987; *Stone et al.*, 1990]. This effect is shown in Figure 3 for a case of pure absorption (i.e., no scattering) in a water cloud derived using Mie calculations for droplet distributions having effective radii of 4, 16, and 64 μm. The BTD^{34} maximum values decrease with increasing effective radius. Particle scattering provides an additional effect on the BTD values. The difference in emittance between the 3.7-μm and the 10.8-μm channels for various surface types (snow, water, land) and water and ice clouds have been used in cloud analyses by *d'Entremont* [1986], *Stone et al.* [1990], and *Allen et al.* [1990]. Other work has been performed using BTD^{45} analysis that exploits the difference in the spectral extinction properties between the IR channels [e.g., *Inoue*,

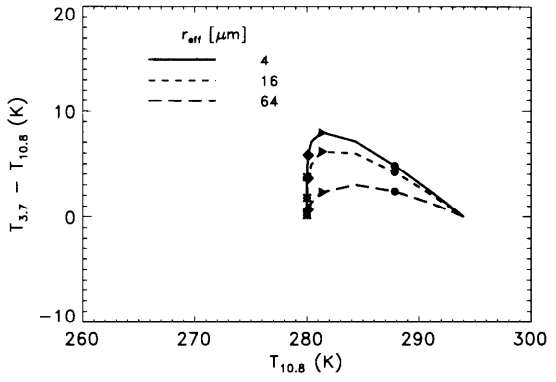

Figure 3. Dependence of water droplet cloud brightness temperature differences on effective radius of cloud particle distribution. For a cloud layer mean temperature of 280 K, results are shown for BTD^{34} ($T(3.7\ \mu m) - T(10.8\ \mu m)$) versus $T(10.8\ \mu m)$. On the theoretical curves, 10.8-μm optical depths of 0.5, 2, 4, and 6 are represented by a circle, triangle, square, and asterisk, respectively.

1985; *Wu*, 1984; *Prabhakara et al.*, 1988; *Parol et al.*, 1991]. *Inoue* [1985] and *Wu* [1984] derived both cirrus cloud temperature and infrared effective emittance and showed that the difference in brightness temperatures between the two channels is greater for thin cirrus than for either optically thick cirrus or for clear-sky conditions. These studies have shown that both the BTD^{34} and the BTD^{45} values are sensitive to the cloud's microphysical and optical properties.

For daytime analysis the interpretation of the upwelling radiances is further complicated by the increase in light scattering by the cloud particles, especially at 3.7 μm. The scattering properties of the cloud are influenced by cloud microphysical properties [*Stone et al.*, 1990], cloud shape, and cloud size [e.g., *Coakley and Davies*, 1986]. This topic is left to a future study currently being performed by the authors.

In section 4 we extend the analyses reviewed in this section relating the dependencies of the BTDs between the AVHRR NIR and the IR channels to cloud microphysical and optical properties and include the effects of particle scattering in the calculations. This investigation differs from previous studies in several respects. First, phase functions for randomly oriented hexagonal ice crystals are used instead of phase functions for spherical particles generated using the Mie theory. Second, calculations are performed for stratus alone, cirrus alone, and cirrus over stratus, i.e., overlapping clouds. The BTD results are shown for both BTD^{34} and BTD^{45} and an intercomparison of results between the two is discussed. Finally, we investigate the effect on BTDs of varying cloud temperature and particle size for overlapping cloud layers.

4. Theoretical Results

Radiative transfer model calculations have been performed for plane parallel cloud layers to infer theoretical BTD^{34} and BTD^{45} values that would result from given cloud particle size distributions and IR optical depths. The radiative transfer calculations are presented in support of the proposed use of satellite radiometer-derived BTD^{34} and BTD^{45} data to infer effective radius and IR optical depth. For each of the figures presented in this and in the following sections, cases were run for a full range of optical depths between 0.1 and 50, although only optical depths of 0.5, 2, 4, and 6 are denoted in the figures. The 10.8-μm optical depths of 0.5, 2, 4, and 6 are represented by a circle, triangle, square, and asterisk, respectively.

4.1. Stratus

The theoretical calculations of BTD^{34} and BTD^{45} are functions of IR optical depth, effective particle size, and 10.8-μm brightness temperature for a single level of stratus cloud. Figure 4 shows the BTD^{34} and BTD^{45} behavior when the stratus temperature and optical depth are varied but the effective radius is held constant. While the stratus 10.8-μm (IR) optical depth varies between 0.1 and 50, symbols representing optical depths of 0.5, 2, 4, and 6 are denoted on the theoretical curves. At low IR optical depths the stratus BTD^{34} and BTD^{45} values are slightly positive due to the increased water vapor absorption at 12 μm relative to 10.8 μm. Water vapor absorption in the 10.8- and 12-μm channels cause the radiative temperature to be below the surface temperature. At higher optical depths the BTD^{34} values become negative while the BTD^{45} values remain positive.

The BTD behavior was reported by, for example, *Hunt* [1973] and *Stone et al.* [1990] to depend on particle size. *Ackerman and Stephens* [1987] used anomalous diffraction theory to predict that particle absorption at 3.7 μm, repre-

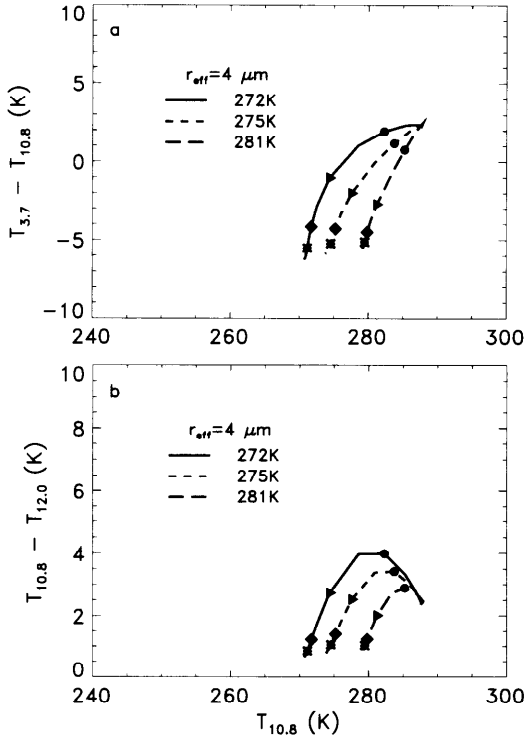

Figure 4. Dependence of stratus cloud brightness temperature differences on mean temperature of stratus cloud layer. Calculations are performed for (a) BTD^{34} ($T(3.7\ \mu m) - T(10.8\ \mu m)$) versus $T(10.8\ \mu m)$ and (b) BTD^{45} ($T(10.8\ \mu m) - T(12\ \mu m)$) versus $T(10.8\ \mu m)$, assuming a stratus particle effective radius of 8 μm. On the theoretical curves, 10.8-μm optical depths of 0.5, 2, 4, and 6 are represented by a circle, triangle, square, and asterisk, respectively.

sented by $(1 - \tilde{\omega}_o)$, increases with increasing effective radius. However, absorption at 10.8 and 12 μm decreases with increasing effective radius. The opposing particle size absorption effects may be used to infer particle size from satellite data. The effects of varying r_{eff} and optical depth are shown in Figure 5 for a stratus deck at 272 K. An increase in r_{eff} acts to increase BTD^{34} values, while BTD^{45} values decrease with increasing r_{eff}. The BTD^{34} and BTD^{45} behavior depend on the nonlinear relationship of the emittance to the different optical properties of the water spheres at the two wavelengths.

Since BTD^{34} values increase and BTD^{45} decrease with increasing r_{eff}, one could infer that the AVHRR 3.7- and 10.8-μm channels are more useful for determining effective particle size for clouds containing large water drops. At high optical depths the BTD^{34} values become negative in sign for r_{eff} of 4 μm and 8 μm but not for the 16-μm distribution. The BTD^{45} values always remain positive in sign. For both BTD^{34} and BTD^{45} calculations the 10.8-μm temperatures asymptote to the cloud temperature as expected.

The theoretical calculations for both cases show that the expected BTD^{34} and BTD^{45} dynamic range is quite small, with both BTD^{34} and BTD^{45} values varying by no more than perhaps 8 K between low and high optical depths.

4.2. Cirrus

The purpose of the calculations involving cirrus optical properties is to determine the range of effective particle sizes

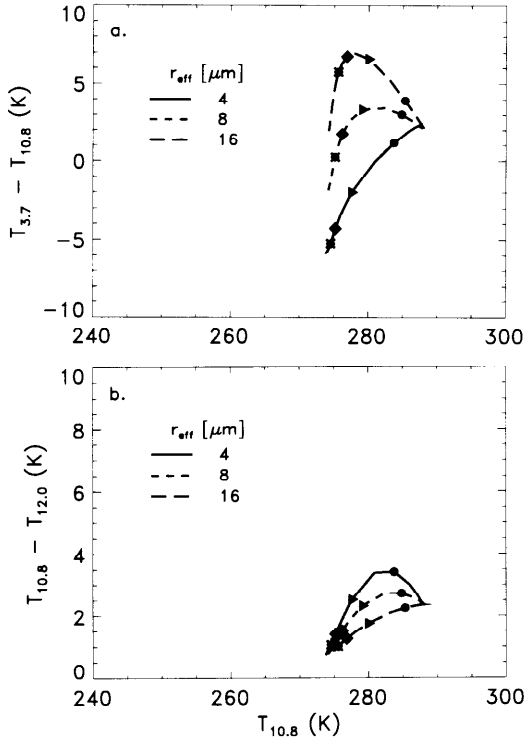

Figure 5. Dependence of stratus cloud brightness temperature differences on effective radius of stratus cloud layer. For a stratus layer mean temperature of 272 K, results are shown for (a) BTD^{34} ($T(3.7\ \mu m) - T(10.8\ \mu m)$) versus $T(10.8\ \mu m)$ and (b) BTD^{45} ($T(10.8\ \mu m) - T(12\ \mu m)$) versus $T(10.8\ \mu m)$. The 10.8-μm optical depths of 0.5, 2, 4, and 6 on the theoretical curves are represented by a circle, triangle, square, and asterisk, respectively.

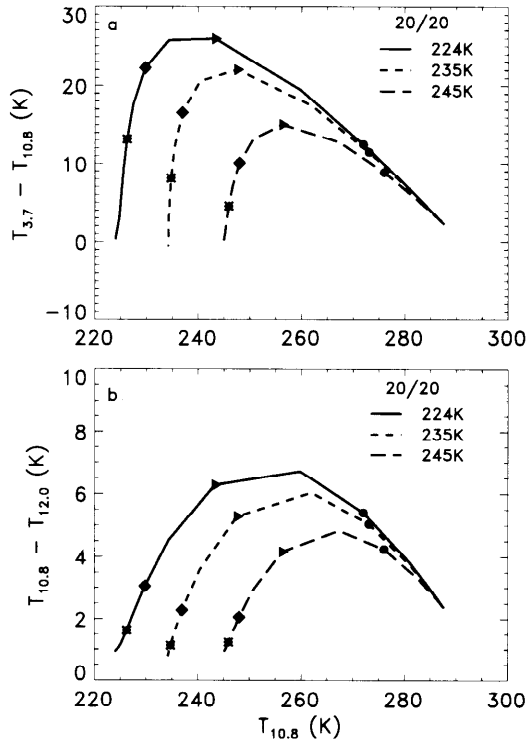

Figure 6. Dependence of cirrus cloud brightness temperature differences on mean temperature of cirrus cloud layer. Results are shown for (a) BTD^{34} ($T(3.7\ \mu m) - T(10.8\ \mu m)$) versus $T(10.8\ \mu m)$ and (b) BTD^{45} ($T(10.8\ \mu m) - T(12\ \mu m)$) versus $T(10.8\ \mu m)$. The 10.8-μm optical depths of 0.5, 2, 4, and 6 on the theoretical curves are represented by a circle, triangle, square, and asterisk, respectively.

and IR optical depths from the AVHRR NIR and IR radiances. Both the spheroidal model for the smaller hexagonal ice crystals and the large-particle model for the larger hexagonal ice crystals are necessary for calculations at NIR and IR wavelengths. Cirrus clouds are assumed to be composed of uniform crystal sizes in the calculations. The effect of varying cirrus cloud temperature on BTD values is presented in Figure 6, which shows the behavior of BTD^{34} and BTD^{45} values as a function of IR optical depth for a cloud composed of size 20/20 hexagonal ice crystals. Actual cirrus clouds are composed of crystals with widely variable shape and size [*Heymsfield and Platt*, 1984]. Recent estimates of cirrus effective radius during the first FIRE cirrus campaign range from 20 μm [*Ackerman et al.*, 1990] to 200 μm [*Wielicki et al.*, 1990]. We will examine a range of hexagonal crystal sizes in the current work, given the lack of better knowledge of cirrus microphysical properties. In this figure we show the cirrus temperature effect on BTD values by placing cirrus at atmospheric layers with corresponding temperatures of 224 K, 235 K, and 245 K. At low optical depths both the BTD^{34} and the BTD^{45} values are positive. As the IR optical depth of the cirrus layer increases, the BTD^{34} values increase until the IR optical depth reaches a value of approximately 2. For thin cirrus the cloud emittance at 3.7 μm is less than at 10.8 μm, so that at low optical depths the cloud appears warmer at 3.7 μm than at 10.8 μm. As the IR optical depth increases above 4, the BTD^{34} values then decrease quickly and the 10.8-μm bright-

ness temperatures asymptote toward the cloud temperature. These results are similar to those reported by *Stone et al.* [1990]. The BTD^{34} curves for the different cirrus temperatures converge to the same clear-sky value of approximately 2 K. The BTD curves for the three cirrus layers converge for IR optical depths below approximately 0.5, indicating that the cirrus BTD^{34} values are relatively insensitive to cloud height at low IR optical depths. For the three cirrus temperatures (224 K, 235 K, and 245 K) used in the calculations, the radiative temperature is within about 1 K of the cloud temperature. The temperature difference may be attributed to scattering within the cloud rather than water vapor absorption since there is very little water vapor above the cloud. The BTD^{34} values for the hexagonal ice crystal distribution do not fall below zero as in the case of the cloud composed of either 4- or 8-μm water droplets for the range of optical depths (0.1 to 50) used here. The dynamic range of the BTD^{34} values is much greater for ice clouds than for water clouds, with a BTD^{34} range of about 24 K compared with 8 K for the water droplet cloud discussed in the previous section.

In comparison with the large BTD^{34} range of values the BTD^{45} values are predicted to be less than approximately 7 K for the cirrus composed solely of 20/20 ice crystal. Typically, BTD^{45} histograms for cirrus scenes have the characteristic shape of an asymmetrical arch. The BTD^{45} is greatest in areas of thin cirrus and least in areas of clear-sky or optically thick cirrus. As shown in Figure 6b, the dynamic range of BTD^{45} values increases as cloud temperature decreases. The maximum BTD^{45} value tends to occur at an IR optical depth of approximately 1 for the three cirrus temperatures. At lower optical depths there is little sensitivity to cloud temperature.

Results are shown in Figure 7 for BTD^{34} and BTD^{45} variations as a function of 10.8-μm brightness temperature for three of the crystal sizes listed in Table 3. Unlike the water droplet cases in Figure 5, both the BTD^{34} and the BTD^{45} values decrease with increasing crystal size. The BTD^{34} values are still much higher than the BTD^{45} values. We also note that the maximum BTD^{34} values shift toward warmer 10.8-μm brightness temperatures as the ice crystal size increases. At low IR optical depths the BTD^{34} values converge to a single line showing that BTD^{34} values are relatively insensitive to cirrus particle size effects at low IR optical depths. At small optical depths the BTD^{45} curves show more variation than is evident from the BTD^{34} curves for the two smallest particle sizes, 20/20 and 50/40. It is also interesting to note that for both the BTD^{34} and the BTD^{45} results, little distinction can be made once particles become larger than 120/60, which corresponds to an area-equivalent sphere having a radius of about 46 μm.

For both BTD^{34} and BTD^{45} results the range of values decrease with increasing particle size. As the size parameter becomes large ($\chi_e \gg 1$), the particles become completely absorbing and the absorption and extinction cross sections at both wavelengths become similar. Consequently, there is a limit to the size particle for which BTD analysis will provide information.

4.3. Cirrus Over Stratus

To investigate the radiance behavior for overlapping clouds, the calculations were also performed for cirrus overlaying a water cloud. In this case, with results shown in Figure 8, the cirrus properties are held constant (T_{uc} = 226 K, 20/20 size particle) and the stratus optical depth is varied between 0.1 and 50. Compared to cirrus alone, both the BTD^{34} and the BTD^{45} values decrease for $\tau_{uc} < 6$ as the lower cloud IR optical depth increases. For the same cirrus optical depth the BTD decreases with increasing stratus optical depth, at least until the lower cloud becomes optically thick and radiates as a blackbody. This is because the maximum difference depends on the thermal contrast between the cloud and its background. For instance, for cirrus with an IR optical depth of 2 overlying stratus with an IR optical depth of 6, the theoretical BTD^{34} is lowered by about 6 K from the case of cirrus over a clear background. Results are not shown for the variation of BTD with cirrus particle size since the results are similar to those shown in Figure 7, where it was shown that BTD values decrease as particle size increases. For cirrus optical depths below approximately 6 the BTD values decrease further for the case when stratus underlays the cirrus layer, and the effect on the BTDs is strongest for cirrus at lower optical depths. The BTD values decrease as the stratus optical depth increases.

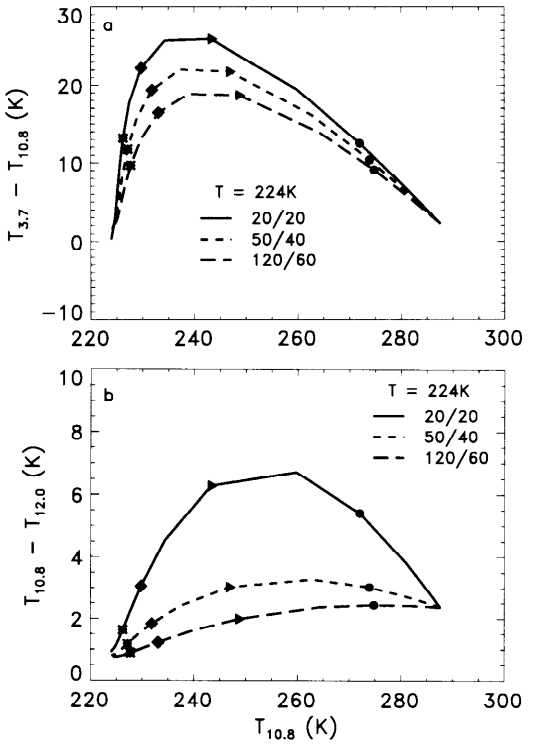

Figure 7. Dependence of cirrus cloud brightness temperature differences on hexagonal ice crystal particle size. Results are shown for (a) BTD^{34} ($T(3.7\ \mu m) - T(10.8\ \mu m)$) versus $T(10.8\ \mu m)$ and (b) BTD^{45} ($T(10.8\ \mu m) - T(12\ \mu m)$) versus $T(10.8\ \mu m)$. The 10.8-μm optical depths of 0.5, 2, 4, and 6 on the theoretical curves are represented by a circle, triangle, square, and asterisk, respectively.

5. Case Study Results

Simultaneous rawinsonde, HIRS, and AVHRR data are used to compare the model calculations with a known multilevel cloud case. These data were taken in the vicinity of Bermuda (located at 32.3°N, 64.7°W) on April 16, 1989, at

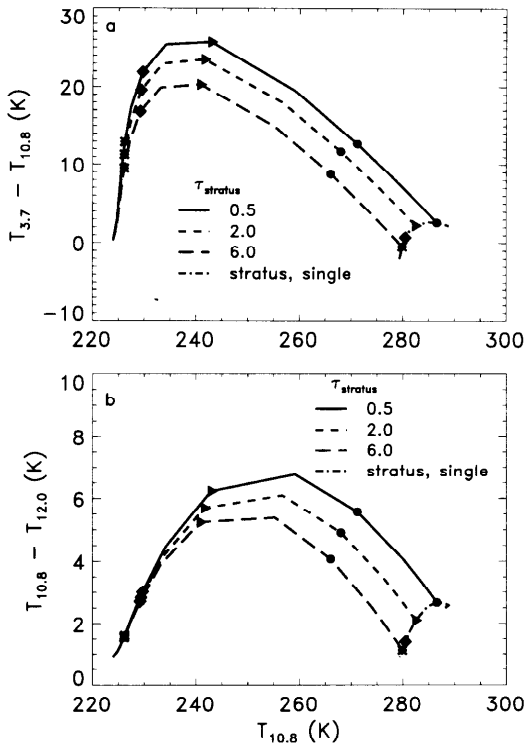

Figure 8. Dependence of cirrus cloud brightness temperature differences on optical depth of underlying stratus cloud layer. Results are shown for (a) BTD^{34} ($T(3.7\ \mu m) - T(10.8\ \mu m)$) versus $T(10.8\ \mu m)$ and (b) BTD^{45} ($T(10.8\ \mu m) - T(12\ \mu m)$) versus $T(10.8\ \mu m)$, assuming a stratus particle effective radius of 8 μm, a stratus mean temperature of 281 K, and a cirrostratus temperature of 224 K. The 10.8-μm optical depths of 0.5, 2, 4, and 6 on the theoretical curves are represented by a circle, triangle, square, and asterisk, respectively.

0606 UTC in support of the First Global Surface Radiation Budget Validation Experiment. The nighttime oceanic multilevel cloud scene under study is presented in Figure 9. In this figure the warm cloud-free ocean is black, the stratus appears as a dark grey, and the colder cirrus varies from white to light grey in color. Meteorological data indicate that between 0000 and 1200 UTC a center of low pressure located off the mid-Atlantic United States coast moved to the east-northeast and rapidly intensified. At the same time, a small strengthening high-pressure ridge moved south, creating a very sharp east-west pressure gradient on the northern edge of the evaluation region (35°N). Over Bermuda, flow veered from light southeast to moderate southwest as a trailing cold front approached the island from the west. Ship reports, although sparse, from the 0000 UTC and 1200 UTC synoptic maps for this time period indicated a variety of cloud types at many levels, including stratiform, cumulus, altocumulus, and cirrus. Figure 10 depicts the temperature (dashed curve) and relative humidity (solid curve) profiles at Bermuda at the time of the NOAA 11 overpass. The technique employed by *Starr and Wylie* [1990] is used to represent the moisture profiles through changing temperature regimes of the troposphere. In this scheme the relative humidity with respect to water is used when $T \geq 0$°C, and the relative humidity with respect to ice is used for $T \leq -20$°C. A linear combination of the relative humidities of ice and water is used in the temperature range between 0°C and −20°C. The humidity values in the atmospheric column exceed 50% with values greater than 75% at around 280 and 450 mbar and from 700 mbar to the surface. We also note that the tropopause is located at approximately 13 km.

The scene in Figure 9 has many interesting aspects, most notably the presence over most of the scene of overlapping clouds. The predominant feature is of a semitransparent cirrus veil overlaying a large low-level stratiform cloud. Three regions shown as rectangles in Figure 9 were chosen for detailed analysis in the following sections.

5.1. Region A Analysis

Region A encompasses Bermuda and contains areas of clear ocean, stratus, and cirrus. Spatial coherence analysis for the stratus region around the edges of the cloud bank shows that the lower cloud brightness temperature is 279–280 K. The physical temperature of the lower cloud top is about 281 K after accounting for water vapor absorption, and the corresponding stratus pressure is about 780 mbar. This result for the lower cloud pressure is corroborated by inspecting the sonde relative humidity data. The sonde data indicate that there is a decrease in humidity at altitudes above about 730 mbar and also a small isothermal layer at that pressure level. If we assume that the absolute lower cloud top resides just below the level where the humidity drops and the temperature inversion starts, then the satellite-retrieved lower cloud pressure is higher than what the sonde data would predict. However, the spatial coherence technique, in assuming that the lower cloud is opaque, retrieves the cloud radiance at the altitude where the cloud appears opaque, and this will be at some distance into the actual cloud.

As shown by *Baum and Wielicki* [1994], the optimal choice of HIRS channels to use with the CO_2 slicing method in a multilevel cloud situation depends upon the height of the upper layer cloud and also upon whether the aim is to reduce bias errors or instantaneous errors. The upper level cirrus in region A are above 10 km, assuming that only a single cirrus cloud layer is present in the HIRS FOV. Since the choice of HIRS channels should be those having weighting functions that peak at or below the cloud, we use the HIRS 4/5 combination to calculate cirrus height and retrieve a mean and standard deviation of 11.2 ± 0.74 km. This result is insensitive to the presence of a low cloud in the HIRS FOV since the transmission is almost nil near the surface in HIRS channels 4 and 5. For illustrative purposes we also present the results using the HIRS 6/7 channel combination; this channel choice is not optimal since the weighting functions for both channels peak well below the cirrus height. If the HIRS 6/7 channels are used, the mean and standard deviations are 10.6 ± 1.0 km, assuming a single level of cloud in each HIRS FOV. However, if the HIRS 6/7 data are evaluated again with the lower surface at 780 mbar, the mean and standard deviation in cloud height are 12 ± 0.6 km. The benefits of using the 6/7 channels are that the cloud signals are much stronger than for the 4/5 channels and also that rms errors due to instrument noise are lower for 6/7 than for 4/5. However, the 4/5 channel selection may be better for retrieval of very high cirrus when overlapping cloud layers are present. As a last result we now calculate cloud pressure from use of only the 10.8-μm HIRS channel and assume that

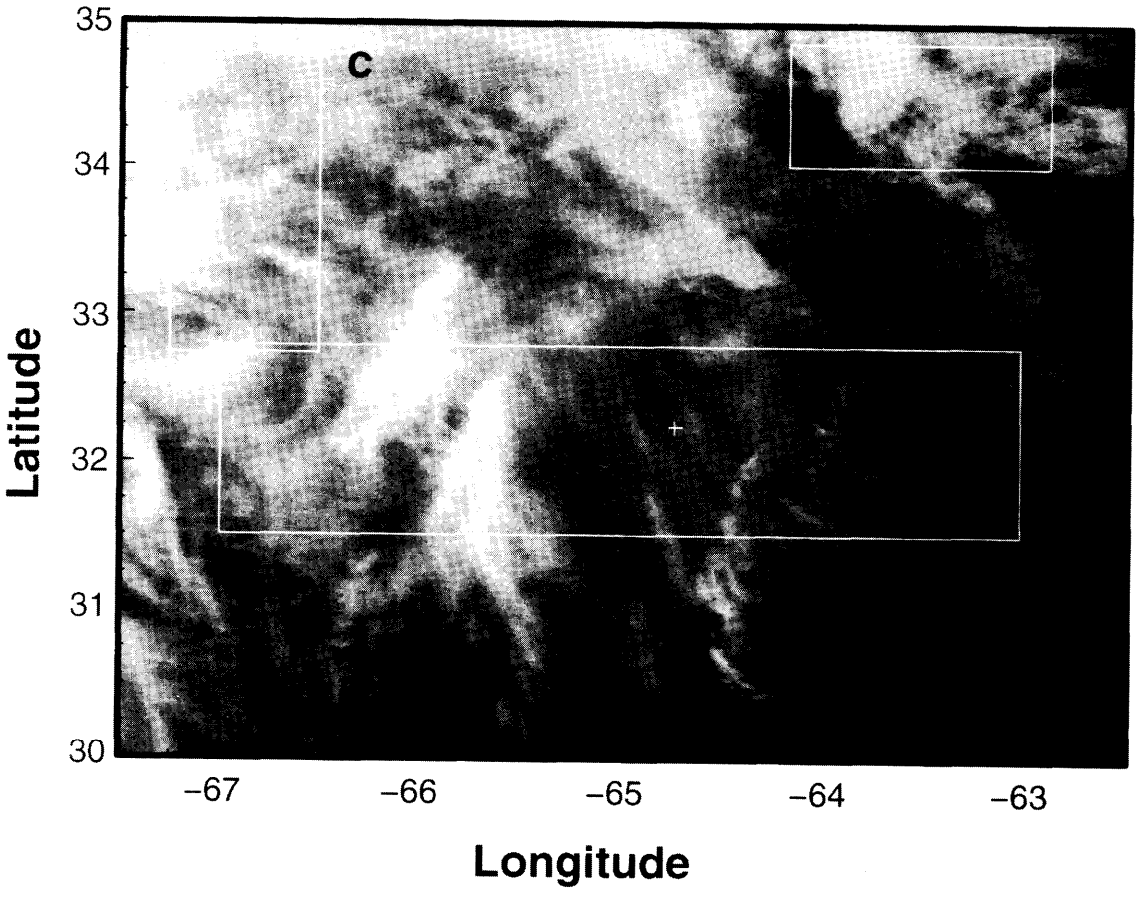

Figure 9. Multilevel cloud scene derived from AVHRR 1.1-km multispectral radiometric data on April 16, 1989, at 0606 UTC.

the cloud is opaque and resides in a single layer in each FOV, with the result that the mean and standard deviation in cloud height is 4.5 ± 1.6 km. This approach is similar to that used for nighttime cloud analysis by ISCCP since only a 10.8-μm channel is available for cloud retrieval. The retrieved 10.8-μm cloud height lies between the upper and the lower cloud layer heights and would lead to a much different interpretation of the radiance fields in radiation and moisture budget analyses.

The proper choice of HIRS channels in the region A analysis eliminates the need for adjusting cirrus height based on the location of the lower stratiform cloud level. However, proper interpretation of the AVHRR NIR and IR data must include consideration of both cloud layers. Figure 11 shows the BTD^{34} and BTD^{45} distribution for the subsampled 1.1-km AVHRR data taken from region A shown in Figure 9. Four curves are superimposed over the data: one corresponding to stratus, one corresponding to single-level cirrus composed entirely of crystals having an aspect ratio of 20/20, and two corresponding to cirrus over stratus. The latter two curves denote cirrus clouds composed of a monodistribution of hexagonal ice crystals having aspect ratios of 20/20 and 120/60. The data following the single-level cirrus curve in Figure 11a show that the IR optical depths are well below 0.5. For the multilevel cloud analysis, we assume low-level stratus cloud properties of $r_{\text{eff},lc} = 8$ μm, $T_{lc} = 281$ K, $\tau_{lc} = 6$, and $T_{uc} = 224$ K. The data presented in Figure 11a indicate that the AVHRR data and theoretical calculations are consistent with the HIRS cirrus analysis and spatial coherence analysis. The BTD^{34} data show that the pixels corresponding to a multilayer cloud situation fall within the range of the two particle sizes and have IR optical depths ranging from near zero to about 4. At optical depths below 0.5 the BTD^{34} data converge, making further interpretation difficult. By comparison, the BTD^{45} data shown in Figure 11b also fall mainly within the range denoted by the 20/20 and 120/60 curves. There are two artifacts present in the AVHRR data shown in Figure 4b. First, the digitization of the AVHRR data causes the points to follow discrete lines from left to right. Second, at a temperature of 275 K there is a discontinuity in the AVHRR data that may partly be due to the temperature dependence of the thermal channel calibration. The thermal channel calibrations are dependent upon the channel central wavenumbers, which are defined as a function of temperature. It is more difficult to distinguish the data corresponding to the single-level cirrus curve in Figure 11b than in Figure 11a. The interpretation of both the BTD^{34} and the BTD^{45} data are reasonably consistent.

The scatter in the data prevents description of the cloud field in terms of a set of curves. The scene is complex and therefore likely to induce a significant spread in the data. Variations in cloud height and thus cloud temperature are probably responsible for some of the scatter. The HIRS analysis shows that over region A the cirrus height ranges from 10 to 12 km. The relatively large HIRS FOV resolution also cannot resolve small-scale cellular features, so the

actual range may be greater. Some data spread may be attributed to variations in ice crystal size. Ice crystal size and habit tend to vary with cloud temperature [*Heymsfield and Platt*, 1984]. Variability in τ_{lc} will give rise to a range in BTD values for constant cirrus conditions. Another potential cause for data scatter is the possibility that the individual AVHRR pixels may not be completely cloud filled. This appears to be a minor issue for much of this scene.

5.2. Region B Analysis

The spatial coherence analysis of region B shows that there is a region of spatial uniformity at a 10.8-μm brightness temperature corresponding to a height of 7.4 ± 0.2 km. The temperature at this height is approximately 251 K after accounting for atmospheric absorption effects. Analysis of the HIRS FOVs in this region using the ratio method with the 6/7 channel combination indicates that the cloud heights span the range 7.8 ± 1.1 km, corresponding to cloud temperatures of 248 K ± 6 K, approximately 3 K lower than the spatial coherence analysis. The HIRS CO_2 slicing analysis and the spatial coherence analysis are reasonably consistent regarding the derivation of the average cloud height and temperature for this region. At a cloud temperature of 251 K, one might expect the cloud to be composed primarily of ice crystals. The following analysis of region B shows that in some cases the BTD analysis may be used to infer phase.

Figure 12 shows the BTD data with overlays of three curves based on theoretical results assuming that the cloud is composed of hexagonal ice crystals with aspect ratios of 20/20, 50/40, or 120/60. The theoretical cirrus optical depths range from 0.1 to 50. The BTD^{34} data shown in Figure 12a would seem to indicate that the best theoretical match is with the 120/60 crystal. However, the BTD^{45} results shown in Figure 12b seem to indicate the presence of smaller particles, not large particles as in Figure 12a. Of interest is that at no point do the theoretical BTD^{34} values in Figure 12a ever fall below zero. The AVHRR BTD^{34} values do become negative, however, and the 10.8-μm brightness temperatures asymptote to the cloud temperature, indicating that the negative values correspond to pixels containing cloud with a high IR optical depth. The BTD^{34} and BTD^{45} results are not consistent with the assumption of cirrus composed of ice particles.

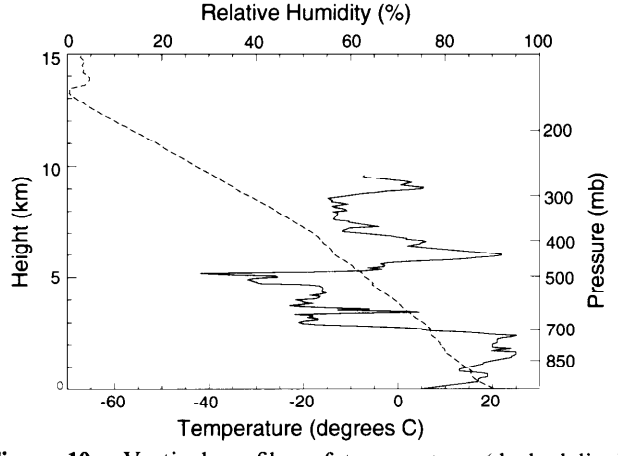

Figure 10. Vertical profiles of temperature (dashed line) and relative humidity (solid line) derived from Bermuda rawinsonde launched at approximately 0500 UTC on April 16, 1989.

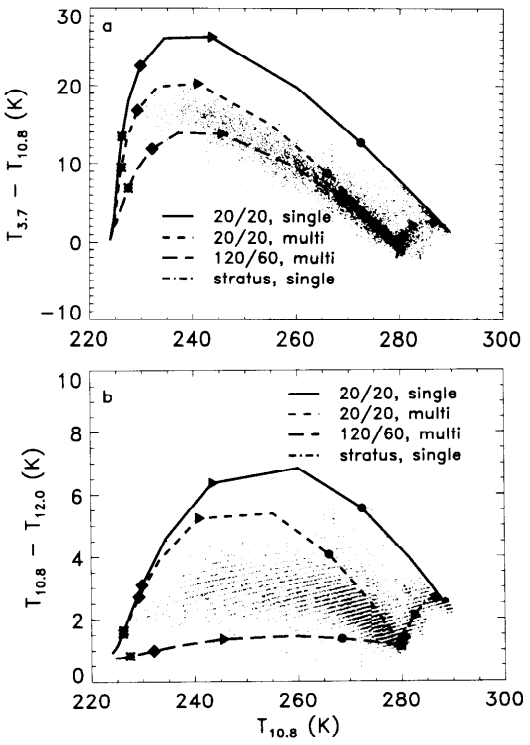

Figure 11. Comparison of theoretical results with AVHRR BTD data from Region A (see Figure 9) for the case of cirrus over a clear background and over a lower-level stratus cloud at T_{lc} = 281 K with r_{eff} = 8 μm. Results are shown for (a) BTD^{34} (T(3.7 μm) − T(10.8 μm)) versus T(10.8 μm) and (b) BTD^{45} (T(10.8 μm) − T(12 μm)) versus T(10.8 μm). The 10.8-μm optical depths of 0.5, 2, 4, and 6 on the theoretical curves are represented by a circle, triangle, square, and asterisk, respectively.

In Figure 13 we now assume that the cloud is composed of supercooled water droplets. Comparison of BTD^{34} data to theory in Figure 13a indicates that the data best correspond to the theoretical curve derived for a cloud composed of a gamma distribution having r_{eff} = 4 μm. In fact, the theoretical results for a cloud composed of water droplets show that the BTD^{34} values should become negative at higher IR optical depths, consistent with the data. Note that the BTD^{34} values never became negative for ice crystal calculations. The BTD^{45} data shown in Figure 13b have maximum BTD values of 8 K but seem to indicate that the r_{eff} range falls between 4 and 8 μm.

5.3. Region C Analysis

The clouds in region C also present a complex radiance pattern. Visual inspection of Figure 9 would seem to indicate that there is a lower cloud underneath the cirrus deck. For this region, spatial coherence analysis does not provide an indication of the presence of low cloud because of the prevalence of thin cirrus. In this situation the spatial coherence technique is likely to provide a large variation in local standard deviations that do not clearly indicate a region of spatial uniformity for either the cirrus or the underlying cloud. However, the BTD^{34} analysis in conjunction with theory does provide evidence for the presence of an underlying cloud layer.

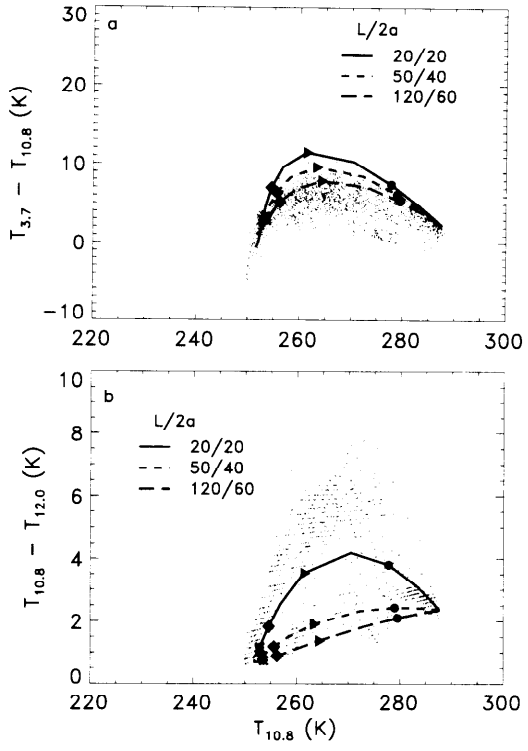

Figure 12. Comparison of theoretical results derived assuming cloud composed entirely of hexagonal ice crystals with AVHRR BTD data from region B (see Figure 9). Results are shown for (a) BTD^{34} ($T(3.7\ \mu m) - T(10.8\ \mu m)$) versus $T(10.8\ \mu m)$ and (b) BTD^{45} ($T(10.8\ \mu m) - T(12\ \mu m)$) versus $T(10.8\ \mu m)$. The 10.8-μm optical depths of 0.5, 2, 4, and 6 on the theoretical curves are represented by a circle, triangle, square, and asterisk, respectively.

The BTD^{34} and BTD^{45} analysis is shown in Figure 14. There are no BTD^{34} and BTD^{45} data at 10.8-μm brightness temperatures above 275 K, and the BTD values are close to zero at 275 K. Since the ocean 10.8-μm brightness temperature is close to 290 K in this region, the only way to explain the data is to assume that a lower-level cloud is present.

The HIRS CO_2 slicing method using the 4/5 channel combination retrieves cloud heights in this region from 10 km to 12.2 km, assuming the presence of the lower cloud at 780 mbar. The mean and standard deviation in cloud height for this region is 11.5 ± 0.6 km, respectively, using the 4/5 ratio. If the HIRS 6/7 combination is used and the radiometric data are interpreted assuming the presence of a lower level cloud in each HIRS FOV, the mean and standard deviation in cloud height is 11.1 ± 0.9 km. If cloud height is retrieved assuming "black" cloud in the 10.8-μm HIRS channel, then the mean and standard deviation in cloud height is 6.7 ± 1.3 km.

The BTD^{34} data provide evidence for at least three cloud layers. In Figure 14 we provide three theoretical curves computed for cirrus over stratus. The cirrus is composed of 20/20 hexagonal ice crystals at 10.8-μm brightness temperatures of 224, 245, and 252 K, or 9.8, 8.5, and 7.5 km, respectively. The stratus curve shown is arbitrary since in this region, there is no area in which the lower cloud appears alone as in region A. For this example, we choose the same stratus properties as in region A of $r_{eff} = 8\ \mu m$ and $T_{lc} = 281$ K. The cloud located at 7.5 km, corresponding to a 10.8-μm brightness temperature of about 252 K, does not show up in the HIRS analysis, possibly due to the lower HIRS FOV spatial resolution and the gap between HIRS FOVs both along a scan line and between scan lines [*Kidwell*, 1991].

To determine how much, if any, of the data spread could be due to cirrus residing at different heights, calculations were performed for cirrus at 224 K for crystal sizes ranging from 20/20 to 120/60. The BTD^{34} results, shown in Figure 15a, show that the data spread cannot be explained by crystal size alone since the theoretical curves do not enscompass the majority of the BTD^{34} data. However, for the BTD^{45} results shown in Figure 15b, much of the data is encompassed by the theoretical curves. It is difficult from inspection of the BTD^{45} data alone to distinguish between clouds residing at different heights and particle size effects. To determine whether cirrus actually resides at different heights instead of a well-defined layer, one would need higher-resolution 15-μm sounding channel data, such as that provided by the HIS instrument or by the moderate resolution imaging spectrometer (MODIS), a facility instrument for the Earth Observing System. The spread of BTD^{45} data shows the difficulty in trying to determine a representative cloud "layer" for each AVHRR pixel. For this region the BTD^{34} data seem to show more clearly that clouds exist at different heights.

As noted in section 4.2, BTD^{45} values are expected to be

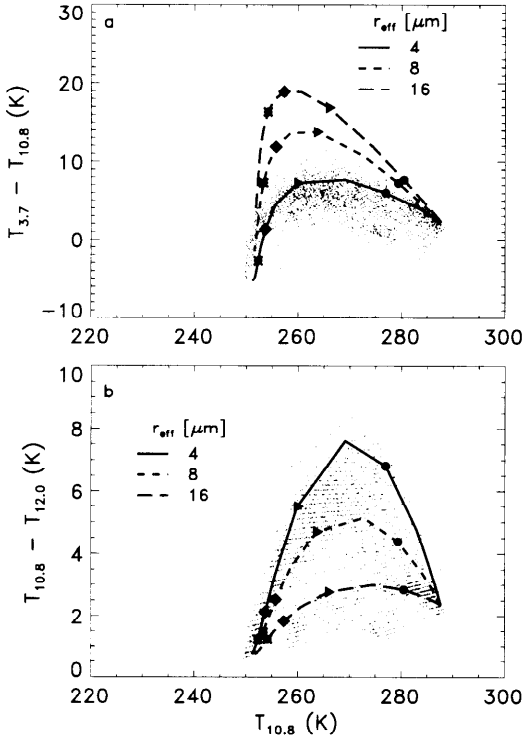

Figure 13. Comparison of theoretical results derived assuming cloud composed entirely of supercooled water droplets with AVHRR BTD data from region B (see Figure 9). Results are shown for (a) BTD^{34} ($T(3.7\ \mu m) - T(10.8\ \mu m)$) versus $T(10.8\ \mu m)$ and (b) BTD^{45} ($T(10.8\ \mu m) - T(12\ \mu m)$) versus $T(10.8\ \mu m)$. The 10.8-μm optical depths of 0.5, 2, 4, and 6 on the theoretical curves are represented by a circle, triangle, square, and asterisk, respectively.

below 7 K for ice particles in single-level clouds. The maximum BTD value will decrease when lower cloud is present. In this example, the maximum theoretical BTD[45] value is approximately 5 K. If the cloud is composed of water droplets, the BTD[45] values may be larger than those expected for ice clouds. In the discussion of Figures 12 and 13 we pointed out that water droplets had a larger relative effect with the BTD[45] calculations than with the BTD[34] calculations. Most of the data are consistent with clouds composed of ice crystals. The relatively large BTD values above 5 K at 10.8-μm brightness temperatures of 255–265 K suggest, however, that some of the clouds are composed of supercooled water droplets.

6. Discussion of Results

A goal of this study is to provide some relatively simple means of distinguishing whether overlapping cloud conditions exist. If overlapping clouds exist, then satellite retrievals of cloud properties must attempt to properly account for both cloud layers. For certain two-level cloud conditions we suggest a methodology that involves both HIRS and AVHRR data to infer the pressure of each cloud level. In order for this methodology to be effective, the cloud layers should cover an area much larger than the HIRS FOV. There are two methods we suggest for determining whether overlapping clouds exist: spatial coherence analysis and brightness temperature analysis. Spatial coherence analysis of the AVHRR radiometric data provides information on whether a low cloud is present. For the spatial coherence analysis it may be necessary to analyze data over more than a 200-km area before finding sufficient low cloud with no overlaying cloud to derive a distinguishable "foot" in the arch. The BTD analysis, in conjunction with theory, also provides clues as to the type of cloud scenario under observation, i.e., water droplet cloud, ice cloud, or overlapping clouds. Application of the CO_2 slicing method to the HIRS 15-μm radiometric data provides independent verification on whether semitransparent cirrus is present in groups of AVHRR data. From this type of analysis it may be possible to conclude in certain instances whether there is a high probability of overlapping cloud layers. Visual inspection of the individual scenes provides an independent check on this procedure.

If two cloud layers exist in a HIRS FOV, we suggest a theoretical means for distinguishing between the two cloud layers. The means to distinguish between two high cloud layers or between high and low cloud involves analysis of the AVHRR (3.7/10.8 μm) and (10.8/12 μm) BTDs. The AVHRR 3.7-μm channel works best when brightness temperatures are higher than approximately 220 K; at lower brightness temperatures the channel may show behavior indicative of digitization or noise problems.

The success of this methodology depends on having well-defined cloud layers at two discrete atmospheric pressure levels and thus different radiating temperature levels.

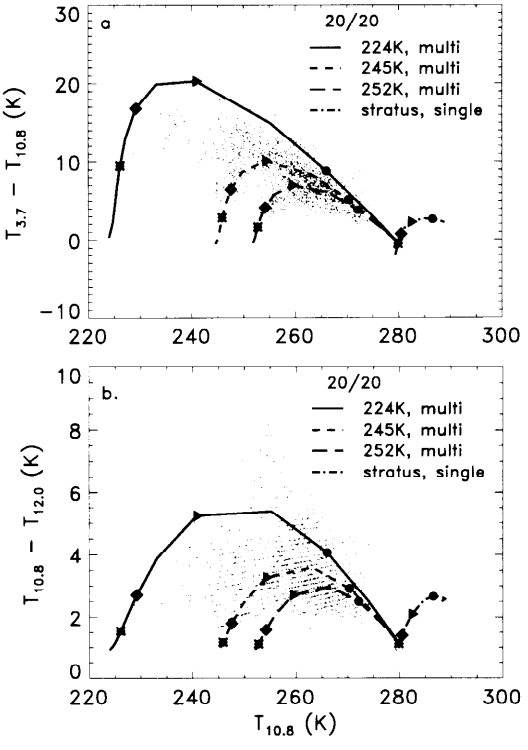

Figure 14. Comparison of theoretical results with AVHRR BTD data from region C (see Figure 9). Results show cirrus temperature effect for (a) BTD[34] (T(3.7 μm) − T(10.8 μm)) versus T(10.8 μm) and (b) BTD[45] (T(10.8 μm) − T(12 μm)) versus T(10.8 μm), for cirrus over lower-level stratus cloud at T_{lc} = 281 K with r_{eff} = 8 μm. The 10.8-μm optical depths of 0.5, 2, 4, and 6 on the theoretical curves are represented by a circle, triangle, square, and asterisk, respectively.

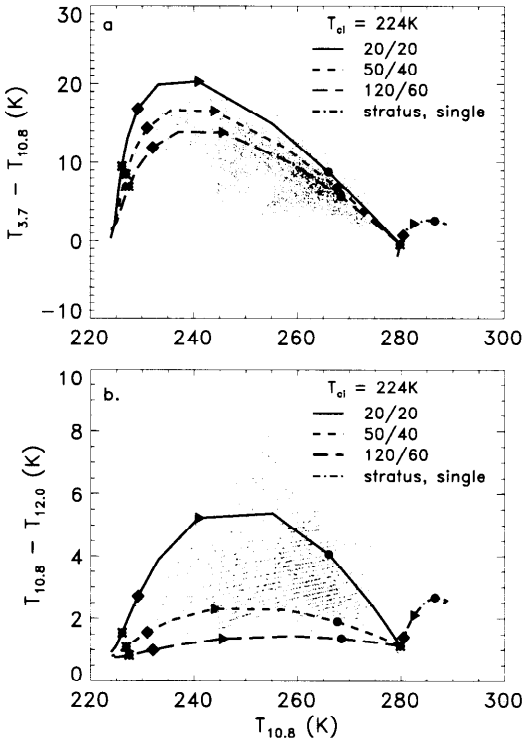

Figure 15. Comparison of theoretical results with AVHRR BTD data from region C (see Figure 9). Results show cirrus particle size effect for (a) BTD[34] (T(3.7 μm) − T(10.8 μm)) versus T(10.8 μm) and (b) BTD[45] (T(10.8 μm) − T(12 μm)) versus T(10.8 μm), for cirrus at 224 K over lower-level stratus cloud at T_{lc} = 281 K with r_{eff} = 8 μm. The 10.8-μm optical depths of 0.5, 2, 4, and 6 on the theoretical curves are represented by a circle, triangle, square, and asterisk, respectively.

The three-level cloud problem has not been discussed in this study because of its complexity. If we are trying to analyze the case of a semitransparent, geometrically thick cirrus layer, the BTD analysis of the AVHRR data may not provide a very clear indication of the nature of the vertical cloud structure. Furthermore, the application of plane-parallel radiative transfer theory to a situation in which clouds exhibit vertical structure assumes that the clouds are horizontally uniform. The BTD analysis of stratiform clouds for the nighttime situation assumed in this study shows the difficulty in distinguishing between variations in cloud particle effective radius and cloud optical depth.

A potential difficulty exists in the spatial coherence analysis of the lower stratus cloud layer. The spatial coherence technique inherently assumes that the lower cloud is optically thick, i.e., the lower cloud radiates as a blackbody. If the lower cloud is not optically thick, then the lower cloud layer may be assigned a higher temperature than it really has, and therefore the cloud will be placed lower in the atmosphere than it should be. Additionally, there may be some difficulty in deriving a distinct low cloud foot if the low clouds are broken and scattered. Errors in the low cloud top pressure would have an impact on the HIRS analysis since a lower surface must be assigned to calculate theoretical upwelling radiances. In using the spatial coherence method, we make the assumption that there will be areas of low cloud that are uncovered by any intervening semitransparent cloud. This assumption may prove to be troublesome if there are not areas in which only the lower cloud is present.

The MSMR technique as presented in this study cannot yet determine with certainty that multilevel clouds may be present in a single HIRS FOV or in any subregion of interest, or that the entire HIRS FOV has a lower cloud layer that completely fills the FOV. In order for this type of method to work in a more automated cloud retrieval scheme, much additional work is necessary to improve the cloud classification. If an automated cloud classification method can provide better information as to whether more than one layer of cloud exists within a group of AVHRR pixels, the potential exists for the methodology proposed in this study to be much more useful in developing global cloud climatologies. Spatial coherence is a simple form of a textural feature. There are additional textural features that could provide information on the composition of a group of pixels [e.g., *Garand*, 1988]. It is likely that textural and spectral features of a cloud scene can be used in conjunction with a set of predefined rules to classify the occurrence of overlapping clouds within a HIRS footprint. This approach is left to a future study.

7. Conclusions

In this study we analyzed a nighttime, oceanic scene in which a cirrus veil overlays a large-scale stratiform cloud and compared the AVHRR NIR and IR radiometric data with theory. The approach that we outlined involves using the spatial coherence method with AVHRR data to determine the low-cloud and clear-sky radiances and the CO_2 slicing method with HIRS 15-μm radiometric data to infer upper cloud pressure. With the use of both AVHRR and HIRS data we can assemble a cross section of the vertical distribution of clouds. Once the vertical distribution of the clouds is inferred, we compare the results of multiple-scattering theory with AVHRR brightness temperature differences between the 3.7-μm and the 10.8-μm channels and between the 10.8-μm and the 12-μm channels to gain further information on each cloud layer's microphysical properties.

The conclusions from this study may be summarized as follows:

1. The MSMR method using both AVHRR and HIRS radiometric data leads to improved interpretation of multilevel cloud scenes over ocean, especially for the case of optically thin cirrus over stratus. The combined use of the spatial coherence method, BTD analysis, and theory provides important evidence as to whether cirrus may be overlying a lower-level cloud.

2. Information on the particle phase, range of particle sizes, and range of optical depths in each cloud layer may be inferred through comparison of theoretical results with AVHRR NIR and IR data.

3. The cloud heights retrieved using only the HIRS 10.8-μm window channel are located between the cirrus and stratiform cloud layers. Use of a 10.8-μm channel is the same as that used by bispectral algorithms, such as ISCCP, for nighttime cloud retrieval. The 10.8-μm channel is insufficient by itself for retrieving multilevel cloud properties. The ISCCP algorithm could benefit by taking advantage of the AVHRR 3.7-μm and 12-μm channels and by inclusion of the HIRS data, both available on the NOAA operational platforms. Although this type of analysis is not possible with most geostationary satellite radiometric data, it would be useful to determine how much of the time-overlapping cloud conditions exist using polar orbiter data.

4. The combined analysis of BTD^{34} and BTD^{45} data provides more information regarding the microphysical properties of the cloud layers than either combination alone.

Finally, we note that this study is only the beginning of an effort to resolve extremely complex but common multilevel cloud occurrences. Even with the potential difficulties we have outlined, the methodology presented in this study provides a framework for beginning to identify and analyze scenes involving more than one overlapping cloud layer. Future work will focus on methods for automating the code and developing additional methods for inferring cloud microphysical properties.

Acknowledgments. The authors gratefully acknowledge K. N. Liou and Y. Takano for providing the hexagonal ice crystal phase functions for the calculations; H. Woolf for providing the HIRS upwelling radiance code; J. A. Coakley, Jr., for providing his spatial coherence code; D. O'C. Starr for providing the sonde analysis technique; and J. Titlow for help in the interpretation of the synoptic maps and analysis of the sonde data.

References

Ackerman, S. A., and G. L. Stephens, The absorption of shortwave solar radiation by cloud droplets: An application of anomalous diffraction theory, *J. Atmos. Sci.*, *44*, 1574–1588, 1987.

Ackerman, S. A., W. L. Smith, J. D. Spinhirne, and H. E. Revercomb, The 27–28 October 1986 FIRE IFO cirrus case study: Spectral properties of cirrus clouds in the 8–12 μm window, *Mon. Weather Rev.*, *118*, 2377–2388, 1990.

Allen, R. C., Jr., P. A. Durkee, and C. H. Wash, Snow/cloud discrimination with multispectral satellite measurements, *J. Appl. Meteorol.*, *29*, 994–1004, 1990.

Baum, B. A., and B. A. Wielicki, Cirrus cloud retrieval using infrared sounding data: Multilevel cloud errors, *J. Appl. Meteorol.*, *33*(1), 107–117, 1994.

Baum, B. A., B. A. Wielicki, P. Minnis, and L. Parker, Cloud

property retrieval using merged HIRS and AVHRR data, *J. Appl. Meteorol.*, *31*(4), 351–369, 1992.
Cess, R. D., et al., Intercomparison and interpretation of climate feedback processes in 19 atmospheric global circulation models, *J. Geophys. Res.*, *95*, 16,601–16,615, 1990.
Chahine, M. T., Remote sounding of cloudy atmospheres, I, The single cloud layer, *J. Atmos. Sci.*, *31*, 233–243, 1974.
Chandrasekhar, S., *Radiative Transfer*, 393 pp., Dover, Mineola, New York, 1960.
Coakley, J. A., Jr., Properties of multilayered cloud systems from satellite imagery, *J. Geophys. Res.*, *88*, 10,818–10,828, 1983.
Coakley, J. A., Jr., and F. P. Bretherton, Cloud cover from high-resolution scanner data: Detecting and allowing for partially filled fields of view, *J. Geophys. Res.*, *87*, 4917–4932, 1982.
Coakley, J. A., Jr., and R. Davies, The effect of cloud sides on reflected solar radiation as deduced from satellite observations, *J. Atmos. Sci.*, *43*, 1025–1035, 1986.
d'Entremont, R. P., Low- and midlevel cloud analysis using nighttime multispectral imagery, *J. Clim. Appl. Meteorol.*, *25*, 1853–1869, 1986.
Downing, H. D., and D. Williams, Optical constants of water in the infrared, *J. Geophys. Res.*, *80*, 1656–1661, 1975.
Garand, L., Automated recognition of oceanic cloud patterns, I, Methodology and application to cloud climatology, *J. Clim.*, *1*, 20–39, 1988.
Gupta, S. K., W. L. Darnell, and A. C. Wilber, A parameterization for longwave surface radiation from satellite data: Recent improvements, *J. Appl. Meteorol.*, *31*(12), 1361–1367, 1992.
Hahn, C. J., S. G. Warren, J. London, R. M. Cherrin, and R. Jenne, Atlas of simultaneous occurrence of different cloud types over the ocean, *NCAR Tech. Note*, *TN-201+STR*, 211 pp., 1982.
Hansen, J. E., and L. D. Travis, Light scattering in planetary atmospheres, *Space Sci. Rev.*, *16*, 527–610, 1974.
Harrison, E. F., P. Minnis, B. R. Barkstrom, V. Ramanathan, R. D. Cess, and G. G. Gibson, Seasonal variation of cloud radiative forcing derived from the Earth Radiation Budget Experiment, *J. Geophys. Res.*, *95*(D11), 18,687–18,703, 1990.
Heymsfield, A. J., and C. M. R. Platt, A parameterization of the particle size spectrum of ice clouds in terms of the ambient temperature and the ice water content, *J. Atmos. Sci.*, *41*, 846–855, 1984.
Hunt, G. E., Radiative properties of terrestrial clouds at visible and infrared thermal window wavelengths, *Q. J. R. Meteorol. Soc.*, *99*, 346–369, 1973.
Inoue, T., On the temperature and effective emissivity determination of semi-transparent cirrus clouds by bi-spectral measurements in the 10 μm window region, *J. Meteorol. Soc. Jpn.*, *63*(1), 88–98, 1985.
Kidwell, K. B., *NOAA Polar Orbiter Data Users Guide*, NOAA National Climatic Data Center, Satellite Data Services Division, Washington, D. C., 1991.
Kneizys, F. X., E. P. Shettle, L. W. Abreu, J. H. Chetwynd, G. P. Anderson, W. O. Gallery, J. E. A. Selby, and S. A. Clough, User's guide to LOWTRAN7, *AFGL-TR-88-0177*, Air Force Geophys. Lab, Bedford, Mass., 1988.
Koenig, E. W., Performance of the HIRS/2 instrument, in *Remote Sensing of Atmospheres and Oceans*, edited by A. Deepak, pp. 67–91, Academic, San Diego, Calif., 1980.
Liou, K.-N., A numerical experiment on Chandrasekhar's discrete-ordinate method for radiative transfer: Applications to cloudy and hazy atmospheres, *J. Atmos. Sci.*, *30*, 1303–1326, 1973.
Liou, K.-N., Y. Takano, S. C. Ou, A. Heymsfield, and W. Kreiss, Infrared transmission through cirrus clouds: A radiative model for target detection, *Appl. Opt.*, *29*(13), 1886–1896, 1990.
McClain, E. P., W. G. Pichel, and C. C. Walton, Comparative performance of AVHRR-based multichannel sea surface temperatures, *J. Geophys. Res.*, *90*(C6), 11,587–11,601, 1985.
McCleese, D. J., and L. S. Wilson, Cloud top heights from temperature sounding instruments, *Q. J. R. Meteorol. Soc.*, *102*, 781–790, 1976.
Menzel, W. P., W. L. Smith, and T. R. Stewart, Improved cloud motion wind vector and altitude assignment using VAS, *J. Clim. Appl. Meteorol.*, *22*, 377–384, 1983.
Menzel, W. P., D. P. Wylie, and K. I. Strabala, Seasonal and diurnal changes in cirrus clouds as seen in four years of observations with the VAS, *J. Appl. Meteorol.*, *31*(4), 370–385, 1992.
Minnis, P., K.-N. Liou, and Y. Takano, Inference of cirrus cloud properties using satellite-observed visible and infrared radiances, I, Parameterization of radiance fields, *J. Atmos. Sci.*, *50*, 1279–1304, 1993.
Parol, F., J. C. Buriez, G. Brogniez, and Y. Fouquart, Information content of AVHRR channels 4 and 5 with respect to the effective radius of cirrus cloud particles, *J. Appl. Meteorol.*, *30*, 973–984, 1991.
Prabhakara, C., R. S. Fraser, G. Dalu, M.-L. Wu, and R. J. Curran, Thin cirrus clouds: Seasonal distribution over oceans deduced from Nimbus-4 IRIS, *J. App. Meteorol.*, *27*, 379–399, 1988.
Ramanathan, V., R. D. Cess, E. F. Harrison, P. Minnis, B. R. Barkstrom, E. Ahmad, and D. Hartmann, Cloud-radiative forcing and climate: Results from the Earth Radiation Budget Experiment, *Science*, *243*, 57–63, 1989.
Schiffer, R. A., and W. B. Rossow, The International Satellite Cloud Climatology Project (ISCCP): The first project of the World Climate Research Programme, *Bull. Am. Meteorol. Soc.*, *64*, 779–784, 1983.
Smith, W. L., and R. Frey, On cloud altitude determinations from high resolution interferometer sounder (HIS) observations, *J. Appl. Meteorol.*, *29*, 658–662, 1990.
Smith, W. L., and C. M. R. Platt, Comparison of satellite-deduced cloud heights with indications from radiosonde and ground-based laser measurements, *J. Appl. Meteorol.*, *17*, 1796–1802, 1978.
Stamnes, K., S.-C. Tsay, W. Wiscombe, and K. Jayaweera, Numerically stable algorithm for discrete-ordinate-method radiative transfer in multiple scattering and emitting layered media, *Appl. Opt.*, *24*, 2502–2509, 1988.
Starr, D. O'C., and D. P. Wylie, The 27–28 October 1986 FIRE IFO Cirrus Case Study: Meteorology and Clouds, *Mon. Weather Rev.*, *118*, 2259–2287, 1990.
Stone, R. S., G. L. Stephens, C. M. R. Platt, and S. Banks, The remote sensing of thin cirrus cloud using satellites, lidar and radiative transfer theory, *J. Appl. Meteorol.*, *29*, 353–366, 1990.
Takano, Y., K.-N. Liou, and P. Minnis, The effects of small ice crystals on cirrus infrared radiative properties, *J. Atmos. Sci.*, *49*, 1487–1493, 1992.
Tian, L., and J. A. Curry, Cloud overlap statistics, *J. Geophys. Res.*, *94*, 9925–9935, 1989.
Tsay, S-C., K. Stamnes, and K. Jayaweera, Radiative transfer in stratified atmospheres: Development and verification of a unified model, *J. Quant. Spectrosc. Radiat. Transfer*, *43*(2), 133–148, 1990.
Warren, S. G., Optical constants of ice from the ultraviolet to the microwave, *Appl. Opt.*, *23*(8), 1206–1225, 1984.
Weinreb, M. P., G. Hamilton, and S. Brown, Nonlinearity corrections in calibration of Advanced Very High Resolution Radiometer infrared chanels, *J. Geophys. Res.*, *95*(C5), 7381–7388, 1990.
Wielicki, B. A., and J. A. Coakley, Jr., Cloud retrieval using infrared sounder data: Error analysis, *J. Appl. Meteorol.*, *20*, 157–169, 1981.
Wielicki, B. A., J. T. Suttles, A. J. Heymsfield, R. M. Welch, J. D. Spinhirne, M. L. C. Wu, D. Starr, L. Parker, and R. F. Arduini, The 27–28 October 1986 FIRE IFO cirrus case study: Comparison of radiative transfer theory with observations by satellite and aircraft, *Mon. Weather Rev.*, *118*, 2356–2376, 1990.
Wiscombe, W. J., Improved Mie scattering algorithm, *Appl. Opt.*, *19*, 1505–1507, 1980.
Wu, M.-L., Radiation properties and emissivity parameterization of high level thin clouds, *J. Clim. Appl. Meteorol.*, *23*, 1138–1147, 1984.
Wylie, D. P., and W. P. Menzel, Two years of cloud cover statistics using VAS, *J. Clim.*, *2*, 380–392, 1989.

R. F. Arduini, Lockheed Engineering and Sciences Corporation, Hampton, VA 23666.
B. A. Baum, P. Minnis, and B. A. Wielicki, Atmospheric Sciences Division, NASA Langley Research Center, Mail Code 420, Hampton, VA 23681-0001.
S.-C. Tsay, NASA Goddard Space Flight Center, Greenbelt, MD 20771.

(Received May 7, 1993; revised September 15, 1993;
accepted October 8, 1993.)